

Single-Frequency Instantaneous GNSS Velocities Resolve Dynamic Ground Motion of the 2016 M_w 7.1 Iniskin, Alaska, Earthquake

by Ronni Grapenthin, Michael West, Carl Tape, Matt Gardine, and Jeff Freymueller

ABSTRACT

Geophysical studies almost exclusively reduce Global Navigation Satellite System (GNSS) observations to positions. Receiver velocities derived from single-frequency high-rate (≥ 1 Hz) carrier-phase observations turn GNSS instruments into velocity meters of unlimited dynamic range, potentially in real time. This enables instantaneous investigation of large, rapid motions. The 125-km-deep M_w 7.1 Iniskin, Alaska, earthquake created only small permanent surface offsets between 1 and 2 cm but much larger dynamic displacements. We resolve S waves and basin resonance, including natural frequencies, using only single-frequency GNSS data without any treatment of error sources along the signal propagation path. Using root mean squared error (rmse) over more than 2.5 min prior to the mainshock as a measure of noise, we determine median rmses for a 36 GNSS station network of 3.1 ± 1.5 , 2.0 ± 0.4 , and 4.8 ± 1.4 mm/s in north, east, and vertical components, respectively. The instantaneous geodetic velocities for the Iniskin event fill observational gaps and allow re-characterization of ground-motion maps for the event. This application demonstrates the utility of geodetic and potentially consumer-grade GNSS receivers for real-time, instantaneous ground motion and site characterization, earthquake early warning, and structural monitoring.

Electronic Supplement: Snapshots of simulated wavefield, kinematic position time series, seismograms and spectrograms, and tables of static offset and peak ground velocity (PGV).

INTRODUCTION

Solid Earth geophysics uses Global Navigation Satellite Systems (GNSS), which include the Global Positioning System (GPS) constellation, to determine and track positions of points on the surface of the Earth in a global reference frame at millimeter precision. Applications include the determination of tectonic plate motion (e.g., Argus *et al.*, 2010), resolution of subsurface magma migration (e.g., Hreinsdóttir *et al.*, 2014), inference of

slip on faults during earthquakes (e.g., Galetzka *et al.*, 2015), and resolution of interseismic strain buildup (e.g., Wang *et al.*, 2001), as well as monitoring of the cryosphere and hydrosphere (e.g., Heki, 2001; Grapenthin *et al.*, 2006; Amos *et al.*, 2014; Borsa *et al.*, 2014).

Over the past 15 yrs, subdaily (e.g., Nikolaidis *et al.*, 2001), high-rate (e.g., Larson *et al.*, 2003; Galetzka *et al.*, 2015), and real-time GNSS (e.g., Grapenthin *et al.*, 2014a) positioning analyses have been developed and have shown the utility of GNSS in real-time hazard analysis and early warning (e.g., Grapenthin *et al.*, 2014b; Melgar *et al.*, 2016). These applications solve the GNSS observation equations for position (equation 1), which require dual-frequency data to correct for ionospheric delay (Misra and Enge, 2011) and are subject to interference of direct and indirect satellite signals (multipath, Choi *et al.*, 2004). High-precision positions also require accurate treatment of several other error terms, including atmospheric disturbances, solid Earth tides, and ocean tides (Misra and Enge, 2011). Sophisticated data processing and application of a series of models are necessary to produce high-quality, subcentimeter position solutions (e.g., Bock and Melgar, 2016). Even with geodetic-quality dual-frequency equipment, real-time positioning precision remains at one to several centimeters, although multi-GNSS approaches promise significant noise reduction (e.g., Geng *et al.*, 2018).

A recent development has been the combination of accelerometers and high-rate GNSS positions to generate seismogeodetic data streams that provide positions at accelerometer frequencies (Bock *et al.*, 2011). This requires collocation of accelerometers at geodetic-quality GNSS stations and resolves earthquake displacements at the temporal resolution of the accelerometer. The technique depends on the alignment of positioning solutions from GNSS and accelerometer data, which are downweighted in the combination to suppress accelerometer drift.

A very different approach involves the estimation of receiver velocities from GNSS carrier-phase observations differenced in time. The technique is well known in geomatics

(Misra and Enge, 2011; Gaglione, 2015) to infer a user's instantaneous velocity. Colosimo *et al.* (2011) showed that coseismic displacements could be inferred when compared with standard solutions by integrating these instantaneous velocities over time. Their method, Variometric Approach for Displacement Analysis Stand-alone Engine (VADASE), provides displacements within a few centimeters when compared with those derived from traditional postprocessed positioning time series. The full version of VADASE uses dual-frequency data and applies simple atmospheric models, but Colosimo *et al.* (2011) also present a simplified single-frequency model. They apply this to L1 and L2 observations in tandem to double the number of observables in the least-squares inversion that estimates receiver velocity and clock bias. Using high-rate data from two GPS stations that recorded the 2011 M_w 9.0 Tohoku earthquake, Branzanti *et al.* (2013) resolve static offsets within 5 cm in horizontal and below 10 cm in the vertical components after integrating the receiver velocities to displacements with the VADASE method. Benedetti *et al.* (2014) compare broadcast orbit-based VADASE solutions, including solutions based on only L1 observations, with several differential and precise point positioning reference solutions for the 2012 M_w 6.1 Emilia earthquake. They show agreement of displacement solutions within 1.7 and 1.8 cm in horizontal and vertical components in the absence of any signal. A comparison between VADASE and displacements retrieved from a triaxial accelerometer, low-pass filtered to match the GNSS sample rates, shows good agreement between the two sensors, demonstrating similar behavior within the same frequency band. Tu *et al.* (2013) demonstrated that a combination of user velocities inferred from single-frequency GPS with a microelectromechanical systems (MEMS) accelerometer enables real-time broadband deformation monitoring. Geng *et al.* (2016) apply the variometric approach to data from the M_w 7.8 Gorkha, Nepal, earthquake, showing ~ 3 and 9 mm/s precision in horizontal and vertical components, respectively, for GPS alone and demonstrate further improvements for multiconstellation solutions (GPS and BeiDou) in the absence of ground deformation.

We derive single-frequency instantaneous GPS velocities, or instavels, as the primary product for the 24 January 2016 M_w 7.1 Iniskin, Alaska, intraslab earthquake (Fig. 1) without further integration to displacements. This estimation uses ultrarapid orbits (low quality, available in real time) and approximate receiver positions from the Receiver Independent Exchange (RINEX) headers only. We do not apply any corrections from models for tropospheric or ionospheric delays because these delays change on longer timescales than the GNSS sample rates of 1–5 Hz used here. Our approach differs from the various VADASE approaches in that we consistently use single-frequency observations and remain in velocity space instead of integrating to displacements. Compared with VADASE, we also do not weight observations based on satellite elevation angle nor apply the Klobuchar ionospheric model (Colosimo *et al.*, 2011; Benedetti *et al.*, 2014).

Our instavels resolve earthquake S waves and basin resonance at more than a 300-km distance from the epicenter,

which show good agreement with velocity records integrated from strong-motion acceleration data for stations within 10- to 50-km distance from the GNSS stations as well as simulated ground motion. We measure peak ground velocities (PGVs) from instavel records and utilize them in the operational ShakeMap setup of the Alaska Earthquake Center to demonstrate their utility (and shortcomings). The method is easy to implement and to apply to data from individual stations. It is readily adaptable to work on real-time data streams, and the resulting velocities could be integrated in source modeling algorithms, which is especially useful in regions of sparse seismic networks. The method requires short-term stable, but not geodetic quality, station monumentation, making it useful for rapid, large-number deployments.

INSTANTANEOUS GNSS VELOCITIES

Instantaneous GNSS receiver velocities exploit the Doppler shift in the carrier-phase observable that results from both satellite and receiver motion. Because the satellite trajectory is smooth, broadcast orbit information is sufficient to estimate and remove the satellite velocity from the observations (e.g., Benedetti *et al.*, 2014; see comparison between ultrarapid and final orbits in $\text{\textcircled{E}}$ Figs. S1 and S2, available in the electronic supplement to this article). The remaining changes in the observed frequency of the satellite signal represent primarily the receiver velocity (Misra and Enge, 2011); residual errors due to orbit or receiver mislocation result in static or low-order polynomial biases, which are easily removed.

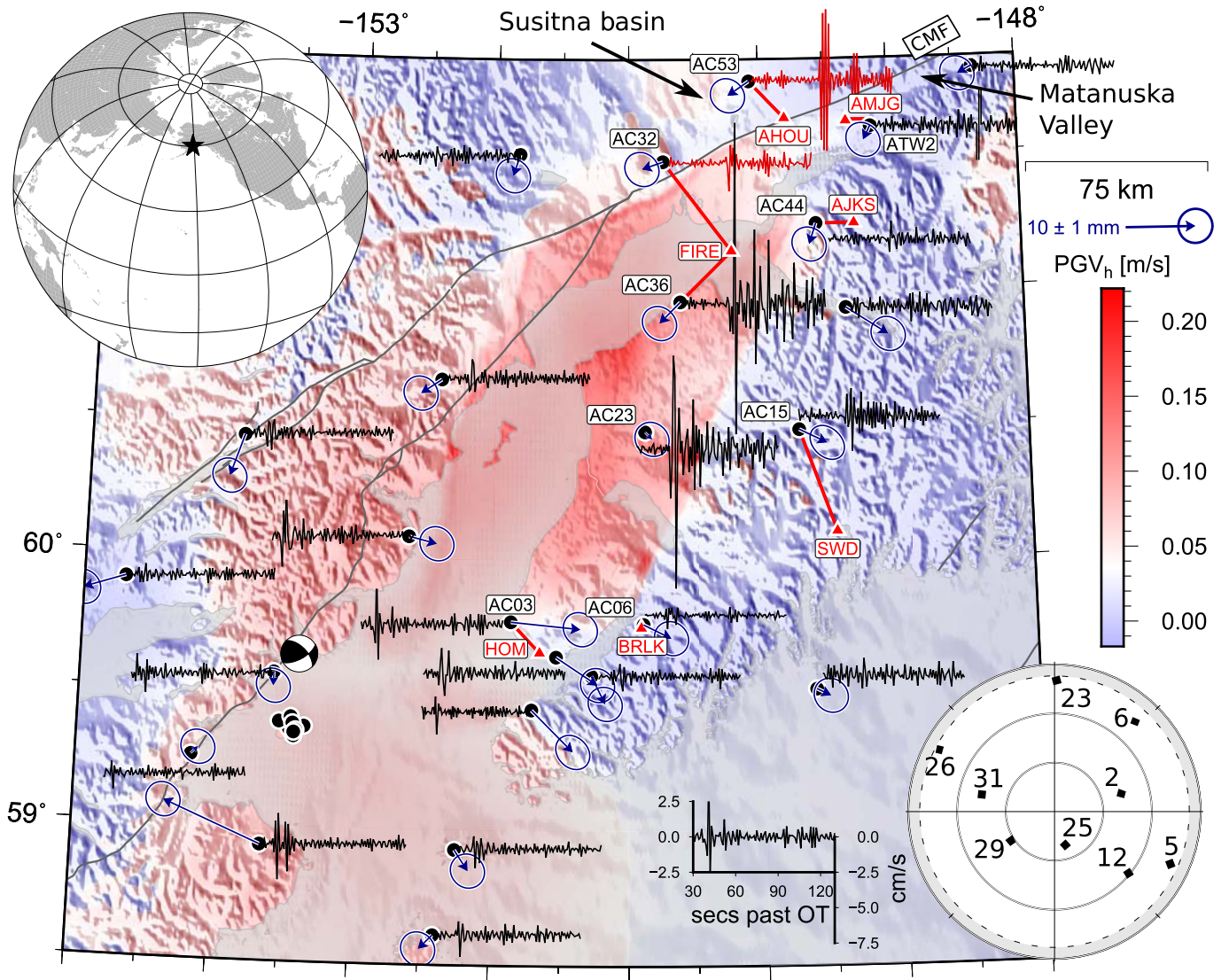
To derive a model for the phase rates, we begin with the phase-observable equation for satellite s

$$\Phi^s = \lambda^{-1}[r - I_\Phi + T_\Phi] + f(\delta t_r - \delta t^s) + N + \epsilon_\Phi \quad (1)$$

(Misra and Enge, 2011), in which λ is the wavelength; r is the range to the satellite; I_Φ , T_Φ are ionospheric and tropospheric propagation delay, respectively; f is the carrier frequency; δt_r , δt^s are receiver and satellite clock bias, respectively; N is the integer number of cycles of the carrier signal; and ϵ_Φ is an error term. It is obvious from equation (1) that differentiation with respect to time—that is, finite-difference approximation using subsequent carrier-phase observations—yields phase-velocity (Doppler shift) observations. This assumes that ionosphere and troposphere are static over short time periods ≤ 1 s and no cycle slips occur. We can express this difference as

$$\Delta\Phi^s = (\mathbf{v}^s - \mathbf{v}_r) \times \mathbf{l}^s + \dot{b} + \delta\epsilon_\Phi \quad (2)$$

(Misra and Enge, 2011; Gaglione, 2015), in which $(\mathbf{v}^s - \mathbf{v}_r) \times \mathbf{l}^s$ is the range difference between the two observations expressed as difference in satellite velocity \mathbf{v}^s and receiver velocity \mathbf{v}_r , projected onto the receiver-to-satellite line of sight with one respective unit vector \mathbf{l}^s . The remaining terms \dot{b} and $\delta\epsilon_\Phi$ are the differenced satellite and receiver clock biases and the differenced error terms, respectively. Correcting the difference between subsequent carrier-phase observations $\Delta\Phi^s$ for average satellite



▲ **Figure 1.** Map of Cook Inlet, Alaska (star in upper left inset shows location), with station locations and Global Navigation Satellite System (GNSS) instavel time series (scale bar to the right). The focal mechanism marks the Iniskin epicenter. Background shows horizontal peak ground velocities (PGVs) (periods ≥ 2.0 s) of the simulated wavefield, revealing the largest amplitudes in Cook Inlet basin (© Text S1, available in the electronic supplement to this article). Black circles are GNSS stations, arrows mark permanent displacements with 95% uncertainty ellipses (© Text S2), and time series are 1 Hz north–south (black) or east–west (AC53, AC32) instantaneous L1–GNSS velocities from 30 to 130 s after the mainshock. Triangles are seismic stations; GNSS and seismic stations connected by lines are compared in Figure 2. Stations named in text or subsequent figures are labeled. Inset in lower right corner shows satellite locations in the sky centered above AC36 around the time of the mainshock. CMF, Castle Mountain fault. The color version of this figure is available only in the electronic edition.

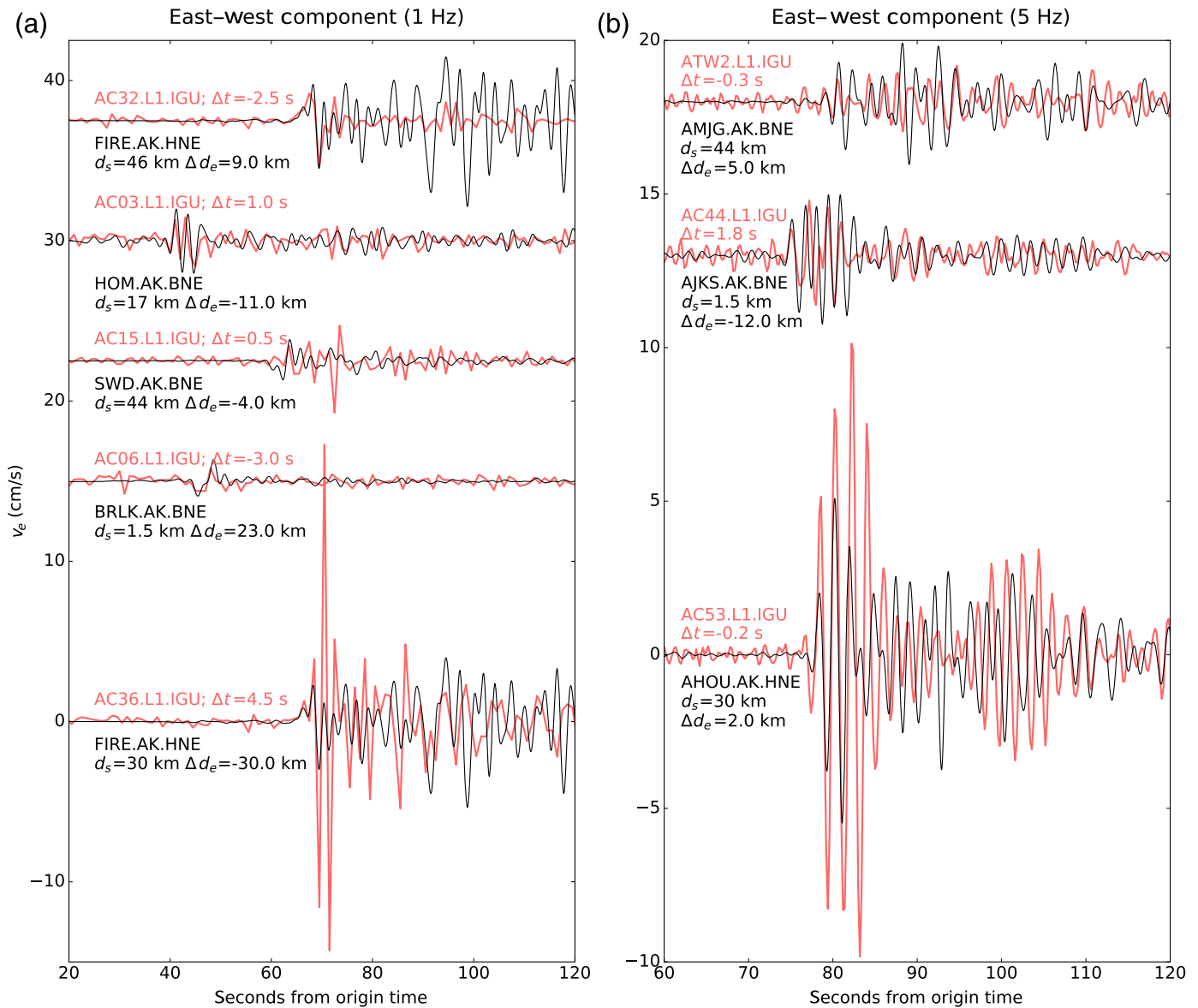
velocity and satellite clock drift between epochs (based on broadcast orbit information or higher quality products in postprocessing) gives a measure of the average Doppler shift D^s of satellite s due to the receiver moving at velocity \mathbf{v}_r :

$$D^s = -\mathbf{1}^s \times \mathbf{v}_r + \dot{b}_r + \delta\epsilon_\Phi. \quad (3)$$

With subsequent carrier-phase observations from at least four satellites, we can set up a linear system of equations with receiver velocity \mathbf{v}_r and receiver clock bias rate \dot{b}_r as model parameters

$$\mathbf{D} = \mathbf{G} \begin{bmatrix} \mathbf{v}_r \\ \dot{b}_r \end{bmatrix} + \delta\epsilon_\Phi, \quad (4)$$

in which \mathbf{D} is a vector of Doppler shift observations and \mathbf{G} is the system matrix that contains unit vectors to project the receiver velocities $\mathbf{v}_r = [v_x, v_y, v_z]^T$ onto the line of sight to the satellite. The receiver velocities are first estimated in an Earth-centered, Earth-fixed Cartesian coordinate system and then rotated into a local east–north–up reference frame. We can solve equation (4) for \mathbf{v}_r and \dot{b}_r using standard least-squares techniques (e.g., Aster *et al.*, 2013). This is similar to the



▲ **Figure 2.** Comparison of L1-GNSS (thick light-colored lines) and strong-motion (thin dark lines) velocities for (a) 1 and (b) 5 Hz GNSS in east-west components. GNSS instavels are aligned to seismic waveforms; respective time shift is given as Δt above the time series. We give distances between the seismic and GNSS station, as well as the difference in their distance from the epicenter as d_s and Δd_e below the seismic station identifier. Strong-motion records in (a) are integrated and filtered between 0 and 0.5 Hz to reflect the frequency content of the 1-Hz GNSS sample rate. Filtering in (b) is between 0.3 and 0.8 Hz (see spectrograms in Fig. 3). Waveforms and amplitudes are generally in good agreement. Differences between AC36 and FIRE reflect basin effects at AC36, which are not expected at Fire Island. The color version of this figure is available only in the electronic edition.

simplified VADASE observation model but removes even the weighting of observations based on satellite elevation angles in the inversion and considers only observations from one frequency, not both in the same inversion.

APPLICATION TO THE 2016 M_w 7.1 INISKIN, ALASKA, EARTHQUAKE

Using ultrarapid orbits provided by the International GNSS service (Dow *et al.*, 2009), we calculate instantaneous velocities

(instavels) for high-rate GPS data (1 and 5 Hz) collected during the 24 January 2016 Iniskin earthquake in Alaska. This M_w 7.1 earthquake ruptured at a depth of 125 km within the subducting slab of the Pacific plate below Cook Inlet. Permanent surface displacements are generally below 2 cm and, given the depth and mechanism of the earthquake, even smaller in the near field (Fig. 1). Although these permanent offsets could be difficult to resolve in kinematic postprocessing, let alone in real time, the much larger dynamic motions due to the S wave are well resolved (Grapenthin *et al.*, 2017). Figure 1

shows time series of instavels that resolve the S wave without saturation, that is, its full dynamic range, as it propagates away from the epicenter. For the entire network of 36 stations with 1-Hz observations, we determine median root mean square errors (rmse) of 3.1 ± 1.5 , 2.0 ± 0.4 , and 4.8 ± 1.4 mm/s in north, east, and vertical components, respectively, for the 2 min, 46 s before the mainshock when the network experiences no motion (starting at 10:28:00 GPS time). The minimum and maximum rmse are 2.2 and 10.7 mm/s in the north component (station AC20 suffered from a slight discontinuity during that time), 1.4 and 3.1 mm/s in the east component, and 3.4 and 9.7 mm/s in the vertical component, respectively. These results degrade at stations where we also have 5-Hz data available. Decimating the 5-Hz observations to 1 Hz before the inversions or filtering of the velocity solutions produces similar observations as the original 1 Hz, so we assume that the additional noise is likely electronic noise from the receiver, which requires future investigation.

To further demonstrate that the retrieved waveforms are reliable, we compare some with nearby strong-motion stations (Figs. 1 and 2). The separation between GNSS site and the closest strong-motion instrument ranges between 10 and 50 km in this region. Although this separation introduces differences due to site effects, these primarily impact high frequencies. (It is helpful to think of the station separation in terms of wavelengths of the filtered waves of interest; at high frequencies, the stations are dozens of wavelengths apart.) Given the constraints imposed by the GNSS sample rates, we compare them with strong-motion records filtered below 1 Hz, which lessens some of the impact of site separation. Figure 2 shows that instavel waveforms generally agree with the strong-motion records, after taking into account the phase shift due to station separation. To highlight similarities and differences in the GNSS and seismic records, we time shifted the instavels so the S -wave arrival aligns with the nearby seismic station (respective shift is given as Δt above the instavel traces in Fig. 2). Although the instavels are noisier, the S -wave arrival and the duration of excitation are clearly captured. Even the small observed ground motions at AC06 and BRLK, (throughout the article, to better distinguish GNSS and seismic stations, we attach a subscript “s” to seismic station identifiers), just outside Cook Inlet basin (Fig. 1), are similar, albeit close to level of noise at AC06. ATW2 and AMJG, agree in the initial part of the excitation. AC53 and AHOU, resolve the same fundamental ground motion within the observed frequencies but differ considerably in amplitude and later in phase. AC53 is amplified by roughly a factor of 2, reflecting its location on 4–5 km of sediments in the Susitna basin (Saltus *et al.*, 2016). Because the waveforms and amplitudes in Figure 2 generally agree and the differences can be explained by site factors, we infer that instavels resolve ground motion within the observed frequency band (below 1 Hz). Both 1- and 5-Hz GNSS capture the dynamic signals, although aliasing due to undersampling occurs at lower sampling rates. This is clear when comparing excitation durations in 1- and 5-Hz records at AC53 (Fig. 3).

Although most currently deployed high-rate GNSS receivers sample at 1–5 Hz, higher frequencies up to 50 Hz are pos-

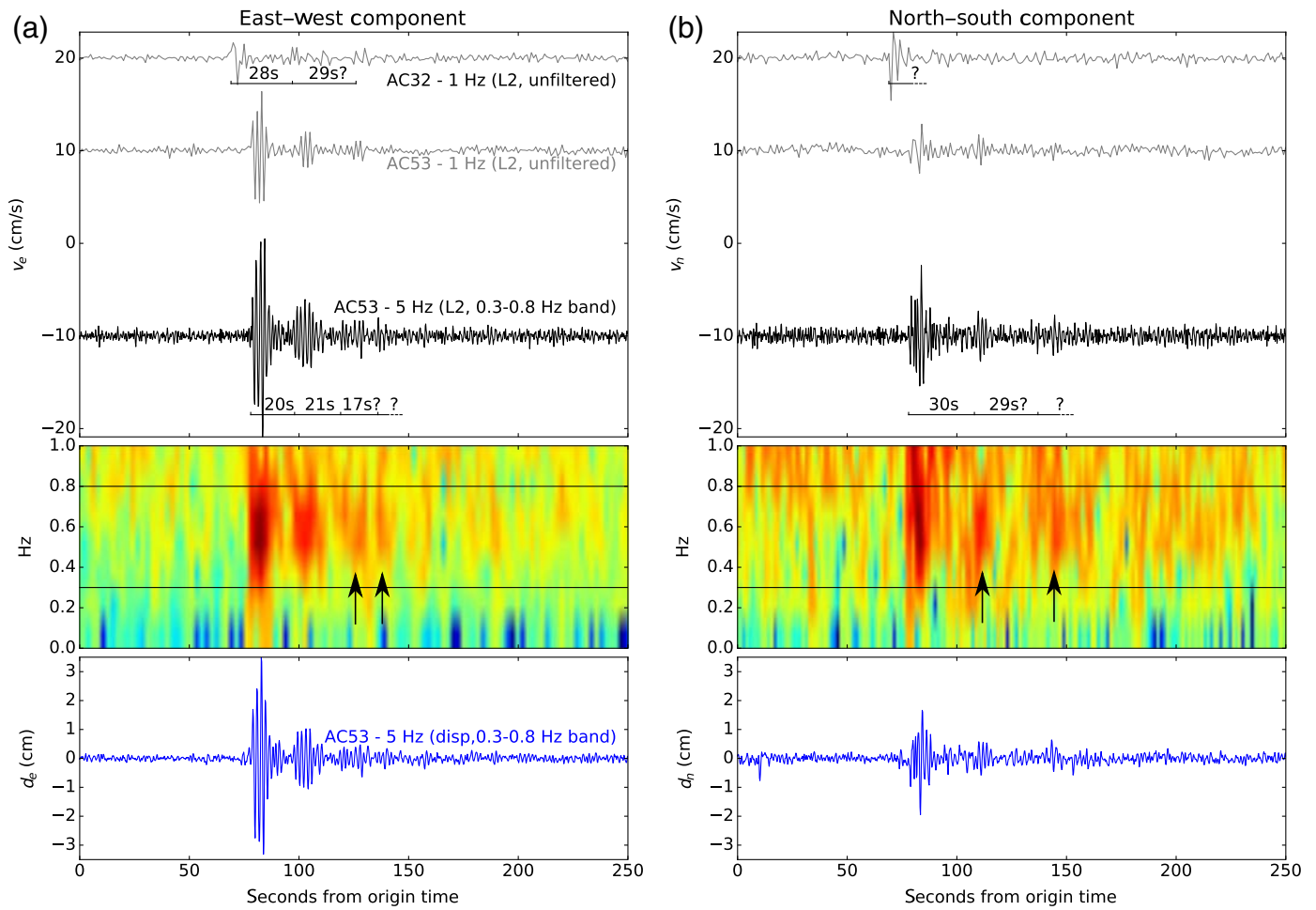
sible. To avoid having to telemeter and store such large data volumes, phase observables could be converted to instavels by solving equation (4) on the GNSS receiver, which is a straightforward operation that requires neither clock corrections nor other model solutions (see also Colosimo *et al.*, 2011).

INTERPRETATION OF THE M_w 7.1 INISKIN INSTAVELS

With confidence in the observations, we can interpret the instavels of Figure 1. The significantly higher velocities and longer excitations of AC23 and AC36 are interesting. These stations are located within Cook Inlet basin, which contains up to 7 km of sedimentary strata (Shellenbaum *et al.*, 2010). Peak instavels of ~ 15 – 24 cm/s are 3–4 times higher than at surrounding stations on bedrock. This demonstrates significant amplification from the basin, in agreement with observed (Fig. 2) and modeled seismic motions (Fig. 1 and © Fig. S3; Text S2).

An intriguing pattern at AC53, AC32 (Fig. 1), and AHOU, (Fig. 2b) is the periodicity in the amplitude envelopes, which suggests repeated constructive and destructive interference of S waves that are reflected off the basin floor and walls. Figure 3 shows east and north velocities at 1 Hz for both AC32 and AC53 and 5 Hz for AC53 only. The 1-Hz instavels reveal that AC32 is subject to lower amplification, but we resolve two or possibly three episodes of excitation, which are about 28 s apart. The location of AC32 on Mt. Susitna, a Tertiary intrusive complex, explains the lower amplitude compared with the basin site AC53. The 1-Hz record of AC53 shows three phases of excitation ~ 20 s apart. However, the 5-Hz record (Fig. 3a, black) reveals that the excitation actually lasts about 5 s longer. This longer lasting excitation is confirmed by the 5-Hz kinematic position time series after filtering between 0.3 and 0.8 Hz (periods 1.23–3.33 s; Fig. 3a and © Fig. S4), which was generated from dual-frequency data, final orbits, and standard corrective models in postprocessing mode (details on the kinematic processing are given in © Text S2). Both AC53’s 5-Hz position solution and the instavels suggest a subtle fourth period of shaking, about 17 s after the third one. Although subtle in the time series, the spectrogram (Fig. 3a, middle panel) confirms the fourth pulse of elevated energy in this pass-band (0.3–0.8 Hz). We find similar, although less pronounced, features in the north component (Fig. 3b, middle panel), where we observe three excitations at AC53 about 30 s apart. The difference in the period of excitation at AC32 and AC53 in the east–west component (Fig. 3a) is possibly due to the width of the basin, which is ~ 130 km at AC32 where the Susitna and Matanuska Valleys join. This assumes that the Castle Mountain fault acts as a waveguide, and hence energy is guided along it between eastern and western valley walls (© Fig. S1). Farther north at AC53, the Susitna basin narrows to about 95 km.

We also determined PGVs at each GNSS site from the instavels—a calculation that could be achieved in real time. Figure 4 shows ShakeMaps generated with the Alaska Earthquake Center’s operational settings from a combination of geodetic and strong-motion PGVs (Fig. 4a). ShakeMaps without basin



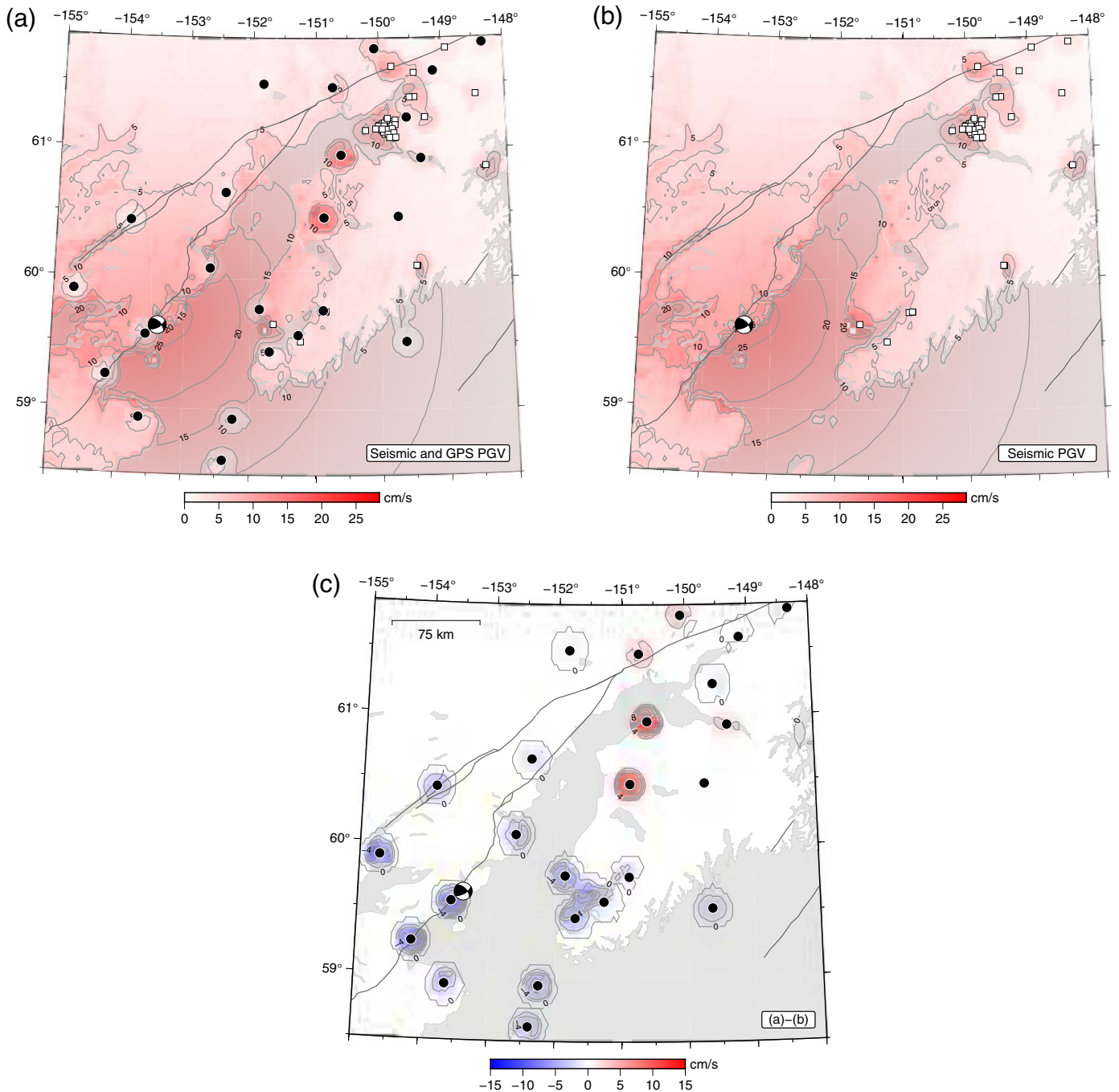
▲ **Figure 3.** (a) East and (b) north components of instavels at AC32 and AC53 (top) and postprocessed kinematic positioning solution at AC53 (bottom). Five-Hz solutions are band-pass filtered between 0.3 and 0.8 Hz. Time series are labeled in (a), with the same order in (b). (a, top) East–west component. Times between oscillations are marked for both stations. AC32 records two or maybe three excitations. AC53 shows three or possibly four excitations at shorter intervals than AC32. (a, middle) Spectrogram of 5-Hz east instavels at AC53 between 0 and 1 Hz. Black lines mark passband for filtering. High-energy content shows four oscillations (with the last two marked with arrows). (b, top) North–south component. AC32 does not present any identifiable oscillations. AC53, in both displacements and instavels, shows three excitations at longer intervals than in the east component. (b, middle) Spectrogram of 5-Hz north instavels at AC53 showing three excitations (with the last two circled) in the passband, with the last one relatively close to noise. The color version of this figure is available only in the electronic edition.

corrections are generated using ground-motion prediction equations from [Zhao *et al.* \(2006\)](#) and V_{S30} data derived from topographic estimation ([Wald and Allen, 2007](#)). We subtract the strong-motion-only ShakeMap ([Fig. 4b](#)) to assess the impact of the geodetic observations ([Fig. 4c](#)). The emerging pattern suggests good agreement of GNSS, strong-motion instruments, and model assumptions in the northern part of the network outside of the basins. Stations AC53, AC32, AC36, and AC23 ([Fig. 1](#)) all indicate higher PGVs than predicted by the ShakeMap model, which does not account for basin sediments. Within 100 km of the source, there is some tendency for the GPS data to underestimate the PGV ([Fig. 4c](#)). As higher frequency ground motion increases near the source, the GPS data are increasingly limited by their 1-Hz sample rate and underestimate the PGV. At the southern tip of the Kenai

Peninsula, AC03 and HOM₁ are 17 km apart. Although their ground motions agree well in the ≤ 1 -Hz range ([Fig. 2](#)), strong *S*-wave energy extends up to 8.5 Hz ([Fig. S5](#)). This suggests that the underestimate is artificially imposed by data sampling and could be avoided using a higher geodetic sampling rate (15–20 Hz) if noise properties similar to those at lower sampling rates can be maintained. Care must be taken in choosing the bandpass when comparing among seismic data, geodetic data, and synthetic seismograms because each of these has different sensitivity at different frequencies.

FURTHER APPLICATIONS

Instantaneous GNSS velocities might have use beyond earthquake characterization. Cheap single-frequency receivers might



▲ **Figure 4.** Impact of GNSS PGVs on ShakeMap. Black circles are GNSS stations, and white squares are strong-motion sensors; real-time settings of the Alaska Earthquake Center are used and explain the imperfect smoothing and circular artifacts. (a) Seismic and GNSS PGVs used together; (b) seismic ShakeMap only; (c) panel (b) subtracted from panel (a). GNSS underestimates of ground velocity close to the source reflect sampling limitations at > 1 Hz. Higher Global Positioning System (GPS) values in northern Cook Inlet are accurate and reveal limitations in the seismic network coverage. The color version of this figure is available only in the electronic edition.

revolutionize our understanding of dangerous and disintegrating terrain, such as glaciers and landslides, by providing an affordable technology for single-use applications.

Large- N citizen science sensor networks (Minson *et al.*, 2015; Kong *et al.*, 2016) could also gain value if single-frequency phase observations are exploited for earthquake and structural monitoring. In particular, the precision of these

observations could increase because neither clock corrections nor other models need to be applied, which also results in minimal processing latency.

Because the precision of instavels rivals postprocessed kinematic GNSS solutions, we propose that these records can readily be used to fill observational gaps in ground motion and structural monitoring and for evaluating site effects using

historical and new GNSS data. This may prove valuable in high-hazard regions where GNSS coverage complements the existing seismic network.


CONCLUSIONS

Instavels derived from single-frequency phase observations can characterize ground motion and site effects and record long-wavelength basin resonance and natural frequencies as expected from seismic observations. Because of its minimal requirements to achieve precise (here $\pm 3\text{--}6$ mm/s) velocity estimates (single-frequency observations, low-quality orbits, nominal positions, no atmospheric, or ionospheric model) this analysis approach will likely have its greatest impact in real-time earthquake analysis, particularly in regions with sparse seismic coverage, and structural monitoring, potentially on board of receivers. Detailed analyses of noise characteristics, particularly their dependence on sampling rate, and the impact of antenna monument quality on performance should be carried out to better assess the limits of this technique.

Our observations of the 2016 Iniskin earthquake fill observational gaps with an unsaturated velocity record to future studies of the earthquake. This is particularly useful because broadband seismometers within 300 km of the epicenter saturated and did not record the full dynamic range of motion. GNSS sampling at rates above 5 Hz may be required to fully capture the dynamics in the near field of earthquakes but may be affected by electronic noise. This may be of particular importance in regions with crustal faults, but as our observations for the 130-km-deep Iniskin earthquake show, may even be required for deeper or far out-of-network events.

Single-frequency instantaneous GNSS velocities may find uses outside of earthquake characterization, particularly in single-use applications in dangerous terrain, or by filling observational gaps in ground-motion assessment. Instavel analysis in large- N sensor networks (e.g., smartphones) could increase the precision while keeping processing latency low.

DATA AND RESOURCES

The original Global Positioning System (GPS) data in Receiver Independent Exchange (RINEX) format are available from UNAVCO. For details on data access, see <https://www.unavco.org/highlights/2016/iliamna.html> (last accessed in August 2016). We used seismic data from the TA (doi: [10.7914/SN/TA](https://doi.org/10.7914/SN/TA)), AK (doi: [10.7914/SN/AK](https://doi.org/10.7914/SN/AK)), and NP networks (doi: [10.7914/SN/NP](https://doi.org/10.7914/SN/NP)) available through the Incorporated Research Institutions for Seismology (IRIS) Data Management Center (DMC). Peak ground velocities (PGVs) were provided by the Alaska Earthquake Center. Generic Mapping Tools (GMT; [Wessel and Smith, 1998](#)) and Matplotlib ([Hunter, 2007](#)) were used for figure creation. 

ACKNOWLEDGMENTS

The authors thank R. M. Allen, S. Bilek, R. Bürgmann, D. Melgar, and M. Floyd for comments on various versions

of the article. Constructive comments from two anonymous reviewers and Editor in Chief Zhigang Peng helped sharpen the article's focus. C. T. was supported through National Science Foundation (NSF) EAR 1215959. This work was supported in part by the high-performance computing and data storage resources operated by the Research Computing Systems Group at the University of Alaska Fairbanks, Geophysical Institute. High-rate Global Positioning System (GPS) data are provided by the Plate Boundary Observatory operated by UNAVCO for EarthScope (NSF EAR 0350028 and NSF EAR 0732947). The sites PBAY and HDPW were established by the University of Alaska, Fairbanks, as part of a National Oceanic and Atmospheric Administration (NOAA)-supported project. The Incorporated Research Institutions for Seismology (IRIS) Data Management Center, funded through the Seismological Facilities for the Advancement of Geoscience and EarthScope (SAGE) Proposal (NSF EAR-1261681), was used for access to waveforms used in this study.

REFERENCES

- Amos, C. B., P. Audet, W. C. Hammond, R. Bürgmann, I. A. Johanson, and G. Blewitt (2014). Uplift and seismicity driven by groundwater depletion in central California, *Nature* **509**, no. 7501, 483–486, doi: [10.1038/nature13275](https://doi.org/10.1038/nature13275).
- Argus, D. F., R. G. Gordon, M. B. Heflin, C. Ma, R. J. Eanes, P. Willis, W. R. Peltier, and S. E. Owen (2010). The angular velocities of the plates and the velocity of Earth's centre from space geodesy, *Geophys. J. Int.* **180**, 913–960, doi: [10.1111/j.1365-246X.2009.04463.x](https://doi.org/10.1111/j.1365-246X.2009.04463.x).
- Aster, R. C., B. Borchers, and C. H. Thurber (2013). *Parameter Estimation and Inverse Problems*, Second Ed., Elsevier Academic Press, Amsterdam, The Netherlands, 360 pp.
- Benedetti, E., M. Branzanti, L. Biagi, G. Colosimo, A. Mazzoni, and M. Crespi (2014). Global Navigation Satellite Systems seismology for the 2012 M_w 6.1 Emilia earthquake: Exploiting the VADASE algorithm, *Seismol. Res. Lett.* **85**, no. 3, 649–656.
- Bock, Y., and D. Melgar (2016). Physical applications of GPS geodesy: A review, *Rep. Prog. Phys.* **79**, no. 10, 106801, doi: [10.1088/0034-4885/79/10/106801](https://doi.org/10.1088/0034-4885/79/10/106801).
- Bock, Y., D. Melgar, and B. W. Crowell (2011). Real-time strong-motion broadband displacements from collocated GPS and accelerometers, *Bull. Seismol. Soc. Am.* **101**, no. 6, 2904–2925, doi: [10.1785/0120110007](https://doi.org/10.1785/0120110007).
- Borsa, A. A., D. C. Agnew, and D. R. Cayan (2014). Ongoing drought-induced uplift in the western United States, *Science* **345**, no. 6204, 1587–1590, doi: [10.1126/science.1260279](https://doi.org/10.1126/science.1260279).
- Branzanti, M., G. Colosimo, M. Crespi, and A. Mazzoni (2013). GPS near-real-time coseismic displacements for the great Tohoku-oki earthquake, *IEEE Geosci. Remote Sens. Lett.* **10**, no. 2, 372–376.
- Choi, K., A. Bilich, K. M. Larson, and P. Axelrad (2004). Modified sidereal filtering: Implications for high-rate GPS positioning, *Geophys. Res. Lett.* **31**, L22608, doi: [10.1029/2004GL021621](https://doi.org/10.1029/2004GL021621).
- Colosimo, G., M. Crespi, and A. Mazzoni (2011). Real-time GPS seismology with a stand-alone receiver: A preliminary feasibility demonstration, *J. Geophys. Res.* **116**, no. 11, 1–14, doi: [10.1029/2010JB007941](https://doi.org/10.1029/2010JB007941).
- Dow, J. M., R. E. Neilan, and C. Rizos (2009). The international GNSS service in a changing landscape of Global Navigation Satellite Systems, *J. Geodes.* **83**, 191–198, doi: [10.1007/s00190-008-0300-3](https://doi.org/10.1007/s00190-008-0300-3).
- Gaglione, S. (2015). How does a GNSS receiver estimate velocity?, *Inside GNSS* (March/April), 38–41.
- Galetzka, J., D. Melgar, J. F. Genrich, J. Geng, S. Owen, E. O. Lindsey, X. Xu, Y. Bock, J.-P. Avouac, L. B. Adhikari, et al. (2015). Slip pulse and

- resonance of the Kathmandu basin during the 2015 Gorkha earthquake, Nepal, *Science* **349**, no. 6252, 1091–1095, doi: [10.1126/science.aac6383](https://doi.org/10.1126/science.aac6383).
- Geng, J., Y. Pan, X. Li, J. Guo, J. Liu, X. Chen, and Y. Zhang (2018). Noise characteristics of high-rate multi-GNSS for subdaily crustal deformation monitoring, *J. Geophys. Res.* doi: [10.1002/2018JB015527](https://doi.org/10.1002/2018JB015527) (in press).
- Geng, T., X. Xie, R. Fang, X. Su, Q. Zhao, G. Liu, H. Li, C. Shi, and J. Liu (2016). Real-time capture of seismic waves using high-rate multi-GNSS observations: Application to the 2015 M_w 7.8 Nepal earthquake, *Geophys. Res. Lett.* **43**, no. 1, 161–167.
- Grapenthin, R., I. A. Johanson, and R. M. Allen (2014a). Operational real-time GPS enhanced earthquake early warning, *J. Geophys. Res.* **119**, no. 10, 7944–7965, doi: [10.1002/2014JB011400](https://doi.org/10.1002/2014JB011400).
- Grapenthin, R., I. A. Johanson, and R. M. Allen (2014b). The 2014 M_w 6.0 Napa earthquake, California: Observations from real-time GPS-enhanced earthquake early warning, *Geophys. Res. Lett.* **41**, no. 23, 8269–8276, doi: [10.1002/2014GL061923](https://doi.org/10.1002/2014GL061923).
- Grapenthin, R., F. Sigmundsson, H. Geirsson, T. Árnadóttir, and V. Pinel (2006). Icelandic rhythmicity: Annual modulation of land elevation and plate spreading by snow load, *Geophys. Res. Lett.* **33**, no. 24, 1–5, doi: [10.1029/2006GL028081](https://doi.org/10.1029/2006GL028081).
- Grapenthin, R., M. West, and J. Freymueller (2017). The utility of GNSS for earthquake early warning in regions with sparse seismic networks, *Bull. Seismol. Soc. Am.* **107**, no. 4, 1883–1890.
- Heki, K. (2001). Seasonal modulation of interseismic strain buildup in northeastern Japan driven by snow loads, *Science* **293**, 89–92.
- Hreinsdóttir, S., F. Sigmundsson, M. J. Roberts, H. Björnsson, R. Grapenthin, P. Arason, T. Árnadóttir, J. Hölmjárn, H. Geirsson, R. A. Bennett, *et al.* (2014). Volcanic plume height correlated with magma-pressure change at Grímsvötn Volcano, Iceland, *Nature Geosci.* **7**, no. 3, 214–218, doi: [10.1038/ngeo2044](https://doi.org/10.1038/ngeo2044).
- Hunter, J. D. (2007). Matplotlib: A 2D graphics environment, *Comput. Sci. Eng.* **9**, 90–95.
- Kong, Q., R. M. Allen, L. Schreier, and Y.-W. Kwon (2016). MyShake: A smartphone seismic network for earthquake early warning and beyond, *Sci. Adv.* **2**, no. 2, doi: [10.1126/sciadv.1501055](https://doi.org/10.1126/sciadv.1501055).
- Larson, K. M., P. Bodin, and J. Gomberg (2003). Using 1-Hz GPS data to measure deformations caused by the Denali fault earthquake, *Science* **300**, no. 5624, 1421–1424, doi: [10.1126/science.1084531](https://doi.org/10.1126/science.1084531).
- Melgar, D., R. M. Allen, S. Riquelme, J. Geng, F. Bravo, J. C. Baez, H. Parra, S. Barrientos, P. Fang, Y. Bock, *et al.* (2016). Local tsunami warnings: Perspectives from recent large events, *Geophys. Res. Lett.* **43**, no. 3, 1109–1117, doi: [10.1002/2015GL067100](https://doi.org/10.1002/2015GL067100).
- Minson, S. E., B. A. Brooks, C. L. Glennie, J. R. Murray, J. O. Langbein, S. E. Owen, T. H. Heaton, R. A. Iannucci, and D. L. Hauser (2015). Crowdsourced earthquake early warning, *Sci. Adv.* **1**, no. 3, e1500036, doi: [10.1126/sciadv.1500036](https://doi.org/10.1126/sciadv.1500036).
- Misra, P., and P. Enge (2011). *Global Positioning System: Signals, Measurements and Performance*, Second Ed., Ganga-Jamuna Press, 569 pp.
- Nikolaidis, R. M., Y. Bock, P. J. de Jonge, P. Shearer, D. C. Agnew, and M. Van Domselaar (2001). Seismic wave observations with the Global Positioning System, *J. Geophys. Res.* **106**, no. B10, 21,897–21,916.
- Saltus, R., R. Stanley, P. Haeussler, J. Jones, C. Potter, and K. Lewis (2016). Late Oligocene to present contractional structure in and around the Susitna basin, Alaska—Geophysical evidence and geological implications, *Geosphere* **12**, no. 5, 1378–1390, doi: [10.1130/GES01279.1](https://doi.org/10.1130/GES01279.1).
- Shellenbaum, D. P., L. S. Gregersen, and P. R. Delaney (2010). Top Mesozoic unconformity depth map of the Cook Inlet basin, Alaska, *Alaska Division of Geological and Geophysical Survey Report of Investigation 2010-2*, doi: [10.14509/21961](https://doi.org/10.14509/21961).
- Tu, R., R. Wang, M. Ge, T. R. Walter, M. Ramatschi, C. Milkereit, D. Bindi, and T. Dahm (2013). Cost-effective monitoring of ground motion related to earthquakes, landslides, or volcanic activity by joint use of a single-frequency GPS and a MEMS accelerometer, *Geophys. Res. Lett.* **40**, no. 15, 3825–3829, doi: [10.1002/grl.50653](https://doi.org/10.1002/grl.50653).
- Wald, D. J., and T. I. Allen (2007). Topographic slope as a proxy for seismic site conditions and amplification, *Bull. Seismol. Soc. Am.* **97**, no. 5, 1379–1395.
- Wang, Q., P.-Z. Zhang, J. T. Freymueller, R. Bilham, K. Larson, X. Lai, X. You, Z. Niu, J. Wu, Y. Li, *et al.* (2001). Present-day crustal deformation in China constrained by Global Positioning System measurements, *Science* **294**, no. 5542, 574–577, doi: [10.1126/science.1063647](https://doi.org/10.1126/science.1063647).
- Wessel, P., and W. H. F. Smith (1998). New, improved version of generic mapping tools released, *Eos Trans. AGU* **79**, 579, doi: [10.1029/98EO00426](https://doi.org/10.1029/98EO00426).
- Zhao, J. X., J. Zhang, A. Asano, Y. Ohno, T. Oouchi, T. Takahashi, H. Ogawa, K. Irikura, H. K. Thio, P. G. Somerville, *et al.* (2006). Attenuation relations of strong ground motion in Japan using site classification based on predominant period, *Bull. Seismol. Soc. Am.* **96**, no. 3, 898–913.

Ronni Grapenthin

Department of Earth and Environmental Science

New Mexico Institute of Mining and Technology

801 Leroy Place

MSEC 356

Socorro, New Mexico 87801 U.S.A.

rg@nmt.edu

Michael West

Matt Gardine

Alaska Earthquake Center

University of Alaska Fairbanks

Fairbanks, Alaska 99709 U.S.A.

Carl Tape

Jeff Freymueller

Geophysical Institute

University of Alaska Fairbanks

Fairbanks, Alaska 99709 U.S.A.

Published Online 11 April 2018